Originally published as:

Atomic scale view on partially molten rocks: Molecular dynamics simulations of melt-wetted olivine grain boundaries

Samia Faiz Gurmani,[1,2] Sandro Jahn,[1] Heinrich Brasse,[2] and Frank R. Schilling[3]

[1] Partial melting is an important geological process that affects physical, chemical and rheological properties of rocks. Here, atomic scale simulations are used to study the structure and transport properties of ultrathin melt films between olivine grains, which is a simple model system of a partially molten peridotite. The model systems consist of 0.8 to 7.0 nanometer thick layers of magnesium silicate melt with a composition close to $MgSiO_3$ confined between Mg_2SiO_4 forsterite crystals. We examine how the atomic structure, the chemistry and the self-diffusion coefficients vary across the interface and investigate their dependence on the thickness of the melt layer and the crystal orientation. Interfacial layers of up to 2 nm thickness show distinctly different physical behavior than the bulk melt and the bulk mineral. The simulation results indicate that for crystal orientations with higher surface energy, the self-diffusion coefficients of all ionic species in the melt decrease. A solid-like charge ordering in the melt is observed close to the crystal-melt interface, which leads to a decrease in mobility of all species. For modeling the petrophysical behavior of partially molten rocks, the effective diameter for the conducting channels is reduced by up to two nanometers, which may effect the rheological and transport properties of the partially molten rocks, especially in the presence of ultrathin melt films in well wetted systems. In the latter case, the electrical conductivity of the confined melt in a partially molten rock could be reduced up to a factor of two due to interfacial effects.

1. Introduction

[2] The existence of partial melts in crustal and mantle rocks has a major influence on their physical, chemical and rheological properties [*Kohlstedt and Holtzman*, 2009]. The process of partial melting is considered very important for the chemical differentiation in the Earth's crust and mantle. The availability of mobile ions as charge carriers makes partial melts a primary source of increased electrical conductivity in the deep Earth.

[3] Electrical conductivity of the asthenosphere is difficult to resolve by deep electromagnetic sounding due to the abundance of high conductivity zones in the crust which blur the image at depth. The clearest indications for an enhanced conductivity originate from cratonic areas [*Eaton et al.*, 2009] and from studies of the oceanic asthenosphere [*Baba et al.*, 2006]. Under favorable conditions, the asthenospheric wedge beneath volcanic arcs may be resolved [*Brasse and Eydam*, 2008].

[4] Systematic experimental studies have been made to get a better understanding of the influence of an existing melt or fluid on rock properties such as seismic velocities or the electrical conductivity. *Schmeling* [1985, 1986] showed that the physical properties of a rock are not only determined by the total amount but also by the distribution of the melt or fluid phase on the grain scale. *Roberts and Tyburczy* [1999] investigated the electrical response of an olivine-basalt partial melt as a function of temperature. The relation of electrical conductivity, degree of partial melting and melt distribution was studied by *Partzsch et al.* [2000]. Electrical conductivity of olivine and its dependence on melt distribution was described by *ten Grotenhuis et al.* [2004, 2005].

[5] The concept of dihedral angle is often used to describe the melt micro-structure and the connectivity of adjacent melt pockets [*Waff and Bulau*, 1979]. Theory predicts that the distribution of melt on the grain boundaries is determined by the difference between interfacial energies of grain boundaries and melt-crystal interfaces [*Waff and Bulau*, 1982]. Subsequent studies have shown that flat crystalline interfaces co-exist with smoothly curved crystal-melt interfaces in equilibrium microstructures of ultramafic partial melts [*Waff and Faul*, 1992] and that a single dihedral angle

---

[1]Section 3.3, German Research Centre for Geosciences, Potsdam, Germany.
[2]Fachrichtung Geophysik, Freie Universität Berlin, Berlin, Germany.
[3]Institut für Angewandte Geowissenschaften, Karlsruhe Institute of Technology, Karlsruhe, Germany.

expression is inappropriate for olivine due to its distinct surface energy anisotropy [*Cmiral et al.*, 1998]. The dihedral angle becomes very small or even approaches zero degrees toward high pressure and temperature in well wetted partially molten peridotite [*Yoshino et al.*, 2009] allowing for very thin melt layers.

[6] *Hess* [1994] showed that the thermodynamics of thin fluid films confined within narrow spaces depends crucially on the film thickness and the film tension. Ultrathin amorphous films (1–2 nm) were found in olivine grain boundaries [*Wirth*, 1996; *Drury and Fitz Gerald*, 1996; *de Kloe et al.*, 2000]. They provide evidence for the existence of thin melt layers in the grain boundaries during partial melting. Chemical analysis across olivine grain boundaries [*Hiraga et al.*, 2003] showed an enrichment of trace elements in an interfacial layer of about 5 nm thickness. *Faul et al.* [2004] studied olivine-olivine grain boundaries in melt-bearing olivine polycrystals and observed a region of about 1 nm thickness that is structurally and chemically different from the olivine grain interiors. The effect of partial melting on the rheology of mantle rocks was reviewed by *Kohlstedt and Zimmerman* [1996] and *Kohlstedt and Holtzman* [2009].

[7] Molecular modeling techniques have been successfully used in many studies to investigate the atomic structure and physical properties of various types of solid-liquid interfaces. This includes classical force field and *ab initio* molecular dynamics simulations of melting behavior of oxides and silicates [e.g., *Belonoshko and Dubrovinsky*, 1996; *Alfe*, 2005] or detailed structural investigations of solid-liquid interfaces of ionic systems [e.g., *Lanning et al.*, 2004]. Confinement effects on melting and freezing of confined material were reviewed, e.g., by *Alcoutlabi and McKenna* [2005] and *Alba-Simionesco et al.* [2006]. Here, we use molecular dynamics simulations to study the behavior of ultrathin MgO-SiO$_2$ melt films confined between Mg$_2$SiO$_4$ olivine crystals as a simple model system of a partially molten peridotite. Using molecular dynamics simulations, we investigate the atomic structure of the solid-melt interface at high temperature and its dependence on the crystal orientation and on the melt layer thickness. We then relate melt structure to transport properties, e.g. the self-diffusion coefficients, and discuss the consequences of melt confinement on the physical properties of partially molten rocks.

2. Computational Details

[8] Molecular dynamics simulations are used to study the atomic scale structure and respective transport properties at the interfaces. With this technique, the time evolution of a set of interacting atoms is followed by numerical integration of the corresponding equations of motion. The properties of interest are extracted from suitable correlation functions and statistical averaging. Molecular dynamics provides direct and simultaneous access to the atomic structure, thermodynamic (e.g. total energy, pressure, P, temperature, T) and transport properties (e.g. self-diffusivity, viscosity, thermal and electrical conductivity).

[9] Here, for the molecular dynamics simulations a time step of 1 fs is used and periodic boundary conditions are applied. The atomic interactions are represented by an advanced ionic model (AIM) that accounts for anion polarization and shape deformations [*Madden et al.*, 2006; *Jahn and Madden*, 2007]. It treats the ions as formally charged, closed shell species. The interaction model is based on four components: charge-charge (Coulomb interaction), dispersion, overlap repulsion and polarization. The overlap repulsion terms allow for spherical "breathing" and dipolar and quadrupole shape deformations of the oxygen ions. The polarization part allows for the induction of dipoles and quadrupoles on the anions (oxygen) due to the electric fields and field gradients of the other ions. The set of AIM potentials used here was parameterized for the Ca-Mg-Al-Si-O system by reference to electronic structure calculations. The model has been shown to be accurate and transferable in a wide range of pressures, temperatures and chemical compositions [*Jahn and Madden*, 2007]. It has been used, e.g., to model the structure and properties of pure forsterite melt [*Adjaoud et al.*, 2008] or high pressure phase transitions in enstatites [*Jahn and Martoňák*, 2008, 2009; *Jahn*, 2010]. More details about the model are given in *Jahn and Madden* [2007].

[10] The $P - T$ conditions of the simulations were chosen to sample the forsterite + liquid two-phase region of the Mg$_2$SiO$_4$−MgSiO$_3$ phase diagram. According to the experimental measurements, the melting temperature of forsterite at ambient pressure is 2163 ± 25 K [*Bowen and Andersen*, 1914] and enstatite melts incongruently at 1830 K to form a silicate rich melt and forsterite [*Lange and Carmichael*, 1987]. At the conditions of our simulations, T = 2000 K and ambient pressure, forsterite coexists with a silicate melt that is slightly enriched in MgO compared to MgSiO$_3$. Starting with a pure MgSiO$_3$ melt, the somewhat different equilibrium melt composition at a given $P - T$ condition is expected to self-adjust in the course of the simulation. Ambient pressure conditions were chosen to allow direct comparison of the obtained transport properties to experimental work on partially molten rocks [e.g., *ten Grotenhuis et al.*, 2005].

[11] The simulation cells of the initial silicate melt (MgSiO$_3$) and of the forsterite crystal (Mg$_2$SiO$_4$) contain a total of 480 ions (96 formula units) and 672 ions (96 formula units), respectively. Solid and melt simulation cells are equilibrated separately. The melt simulation cell is equilibrated for 50 ps in the *NPT* ensemble (constant number of particles, pressure and temperature) using an isotropic barostat [*Martyna et al.*, 1994] coupled to a Nosé-Hoover thermostat [*Nosé and Klein*, 1983]. Similarly, the forsterite simulation cell is equilibrated at the same conditions in the *NPT* ensemble but using an anisotropic barostat keeping the simulation cell orthorhombic. After equilibration, the barostat is switched off and production runs of 250 ps length for the solid and 500 ps length for the melt are started in the *NVT* ensemble (constant volume). The results of both simulations are used as reference to represent the structure and properties of the bulk crystal and the bulk melt.

[12] After solid and melt are equilibrated separately, interfaces are constructed between them as follows. First, the crystal cells are rotated to yield three different surface terminations: (010), (100) and (001). Then, four different melt layers are constructed by using 1 × 1 × 0.5, 1 × 1 × 1, 1 × 1 × 2 and 1 × 1 × 4 supercells of the melt simulation box. The 1 × 1 × 0.5 cell with 240 ions was re-equilibrated after removing half of the ions from the cubic box and
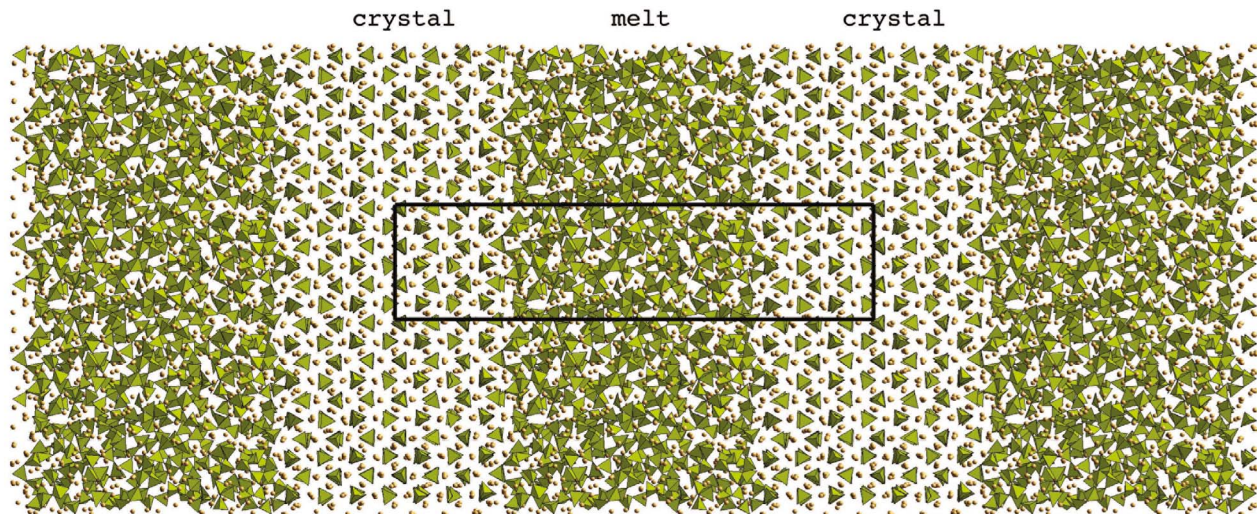
Figure 1. Snapshot from simulation of interface C with (010) crystal surface termination. SiO_4 tetrahedral units and Mg ions are shown in polyhedral representation and as balls, respectively. Black lines indicate the simulation box, which is about 7 nm long and periodically repeated in three dimensions. Thus, the model is composed of alternating melt (disordered) and crystal (ordered) layers.

reducing the simulation cell length in one dimension. The different melts are subsequently confined between two crystal cells (2×672 ions) leaving a small gap (0.1 nm) between melt and solid to avoid direct ion contacts. To overcome the misfit in the cross-section between melt and crystal, the particle positions in the melt are rescaled in the interfacial plane. Thus, 12 different solid-melt interfaces with three different surface terminations and four different melt thickness layers are obtained. In the following, we refer to interfaces containing initial melt layer thicknesses of 0.8 nm, 1.6 nm, 3.3 nm and 6.5 nm as A-, B-, C- and D-interfaces. The total numbers of ions in these supercells are 1584, 1824, 2304 and 3264, respectively.

[13] All interfaces are equilibrated at ambient pressure and 2000 K for 50 ps in the *NPT* ensemble. The gaps are closed during equilibration within few starting steps. Due to the different interfacial cross sections of the orthorhombic crystal cell in different orientations, the resulting thickness of the melt layers after equilibration varies slightly between interfaces with different surface terminations but with the same number of melt atoms (see Table 3).

[14] After equilibration, production runs of 700 ps length for all interfaces are collected in the *NVT* ensemble. A snapshot from the simulation of interface C with (010) crystal surface termination in shown in Figure 1. From the particle trajectories we derive various properties like charge density, cation coordination, connectivity of SiO_4 tetrahedra and self-diffusion coefficients. For a detailed analysis of the various

properties across the interface, the simulation cell of each interface is divided into layers parallel to the interface. More details are given in the following section.

3. Results

3.1. Bulk Structure and Free Surface Properties

[15] For reference, we first present some structural properties of the bulk crystal. As already shown in a previous study [*Jahn and Madden*, 2007], the AIM potential predicts the forsterite structure in good agreement with experimental data [*Fujino et al.*, 1981]. The corresponding lattice constants at ambient conditions are compared in Table 1. Similarly, the elastic constants, the thermal expansion at ambient pressure and the volume compression under applied pressure are well reproduced [*Jahn and Madden*, 2007].

[16] The free surface energies of three surfaces (100), (010) and (001) of forsterite were calculated. For each surface, the crystal is cut under the condition of a zero dipole perpendicular to the surface since a resulting dipole in a periodic cell would lead to a divergent surface energy [*Bertaut*, 1958]. The surface terminations and the relaxation process are similar to those used by *Watson et al.* [1997]. In Table 2, the surface energies obtained from the AIM potential are compared to the results of the previous simulation study by *Watson et al.* [1997] using a rigid ion model. Despite relative differences of up to about 20% in the surface energies due to the different interaction potentials, both

Table 1. Lattice Parameters of Forsterite From Experiment at Ambient Conditions [*Fujino et al.*, 1981] and AIM Simulations at $T = 0$ K [*Jahn and Madden*, 2007]

	Experiment	AIM
a (Å)	4.75	4.73
b (Å)	10.19	10.19
c (Å)	5.98	5.95

Table 2. Free Surface Energies (in J/m^2) of Forsterite Calculated for Three Surfaces by AIM and a Rigid Ion Model [*Watson et al.*, 1997]

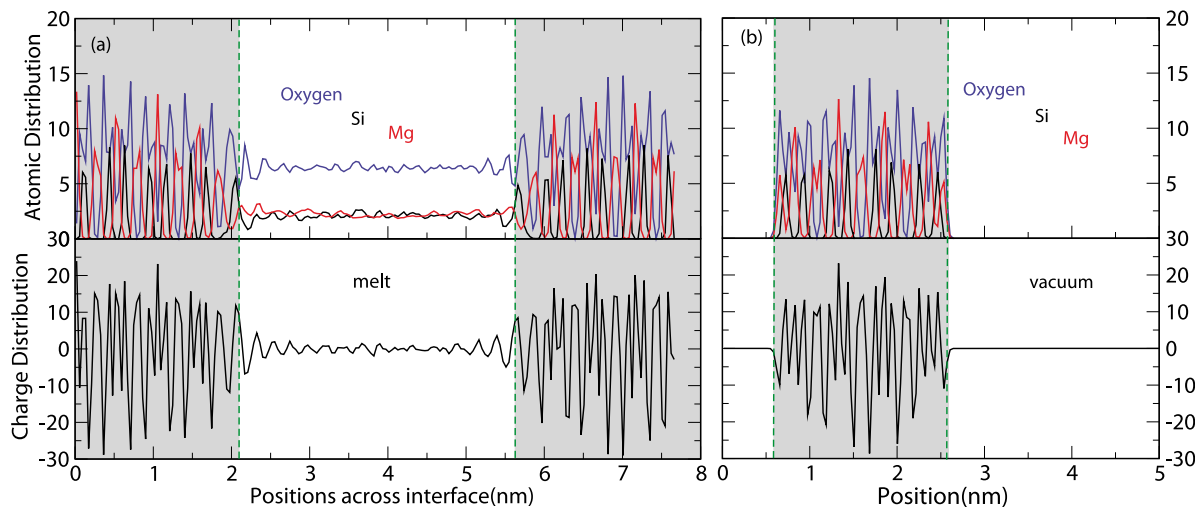| Surface	Present Study	*Watson et al.* [1997]
(100)	2.21	2.02
(010)	1.27	1.28
(001)	1.89	1.61

Figure 2. Average (top) atomic and (bottom) charge distribution profiles across (a) interface C with (010) crystal orientation and (b) the relaxed free (010) surface of forsterite. The vertical dashed lines on each profile show the initial interface. Grey and white areas represent the crystal and the melt (vacuum) part of the simulation cell.

models agree in that the most stable surface is (010) because it has the lowest surface energy. Both models predict the highest surface energy for the (100) surface whereas that of the (001) surface is somewhat lower.

3.2. Structural Properties of the Interfaces

3.2.1. Density Profiles

[17] Variations of the structure across the interfaces may be represented by the charge and the atomic density profiles. As an example, the distribution of the different elements (Mg, Si, O) across interface C with (010) crystal orientation is shown in Figure 2a (top). These profiles are an average over the total production run of 700 ps. The spacial resolution after dividing the simulation cell into 200 layers is about 0.04 nm. Green vertical lines and grey areas represent the position of the original interface and the original crystal. The total charge distribution, shown in Figure 2a (bottom), is obtained by counting all atoms in the respective layer multiplied by their respective charges. This function oscillates around zero due to charge neutrality of the whole simulation cell. The strong oscillations in the crystal part on both sides are due to the periodic crystal structure. A relatively strong solid-like charge ordering is also observed in the first melt layers close to the mineral-melt interface.

[18] The effect of the melt on the crystal surfaces is apparent from the comparison of the interfacial element and charge distribution profiles (Figure 2a) with the corresponding profiles of the free surface, i.e. the crystal surface in contact with vacuum (Figure 2b). The latter show much less reconstruction or distortions from the bulk structure close to the interface than the crystal surfaces in contact with the melt. The atomic and charge distribution functions for the solid-melt interfaces suggest an interfacial width with strong deviations from the bulk behavior of about 1–2 nm. However, there are still small oscillations even in the central part of the melt, which are due to the strong electrostatic ordering effect arising from the crystal structure. Interfaces B and D show similar small oscillations in the center of the

melt, whereas the oscillation amplitudes are larger for interface A due to the smaller thickness of this melt layer.

3.2.2. Chemical Composition

[19] On the atomic scale, wetting of the crystal surface by the silicate melt leads to chemical heterogeneities in the interfacial region. For interface C with (010) crystal orientation, the simulation cell is divided into 120 layers and the respective chemical composition of each layer in terms of MgO and SiO_2 components is shown in Figure 3. The immediate contact between crystal and melt is characterized by strong compositional fluctuations. The atomic layers of the crystal close to the interface are somewhat enriched and the average melt composition is slightly depleted in SiO_2 component. As already mentioned earlier, the phase diagram suggests a MgO mole fraction above 0.5 for the melt under
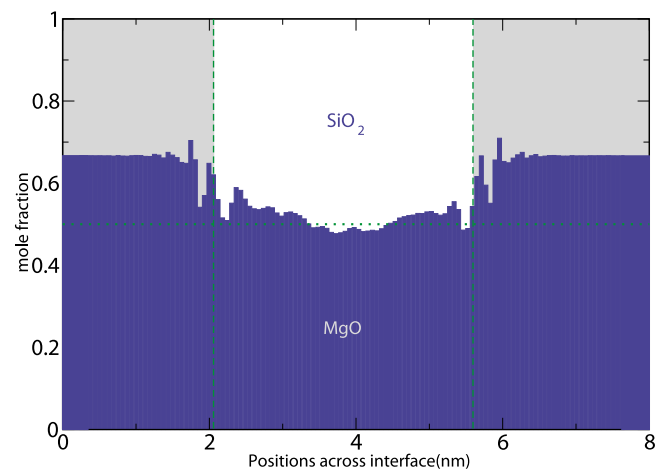

Figure 3. Chemical composition across interface C with (010) crystal orientation in terms of MgO and SiO_2 components. The horizontal dotted line indicates $MgSiO_3$ composition.
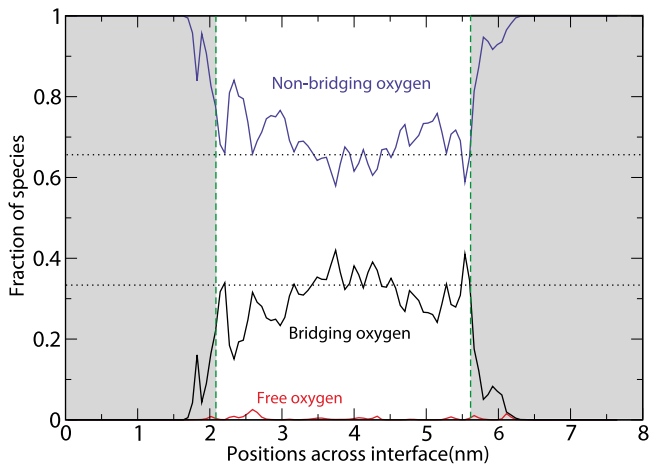
Figure 4. Fractional distribution of oxygen coordinations by silicon as a function of position across interfaces C of (010) crystal surface termination.

the $P - T$ conditions studied here, which seems to be consistent with the simulation results.

3.2.3. Coordination

[20] The coordination of an atom i was determined by counting all atoms of a given species j within a sphere of a cutoff radius. The latter is defined by the first minimum in the respective radial distribution function $g_{ij}(r)$. The coordination profiles of oxygen by silicon are shown in Figure 4 for (010) crystal orientation of interface C. Bridging oxygens are defined as having two nearest neighbors of silicon, whereas non-bridging oxygens have only one. There are also a few free oxygens with no nearest neighbor Si. Horizontal lines represent the nominal distribution according to the formula $MgSiO_3$, in which 2/3 of the oxygens are non-bridging and 1/3 are bridging oxygens. The olivine crystal (Mg_2SiO_4) has only non-bridging oxygens, which can be seen in the crystal part of Figure 4.

3.3. Self-Diffusion Coefficients

[21] Self-diffusion coefficients are calculated from the slope of mean square displacements of ions over a given time t [Allen and Tildesley, 1987]

$$2tD = \frac{1}{3}\left\langle (r_i(t) - r_i(0))^2 \right\rangle \tag{1}$$

where D is the self-diffusion coefficient, t is the time, $r_i(t)$ is the position of particle i at time t, and brackets refer to an average over time and ions of the same species.

[22] For all interfaces, the self-diffusion coefficients are calculated by two methods. In the first case, all atoms that were contained in the original melt before constructing the interface are considered in the averaging of the mean square displacements. A time average is performed over 500 ps of the production runs.

[23] In the second case, the interface is divided into 10, 15, 20 and 30 equidistant layers for the A, B, C and D interfaces, respectively. To account for interdiffusion between the layers, the time average over the mean square displacements is constrained to intervals of 100 ps. This means that for production runs of 700 ps, there are seven intervals of 100 ps.

The assignment of atoms to individual layers is made at the beginning of each 100 ps interval. Finally, an average over the seven intervals is taken. Self-diffusion coefficients of all three species are averaged over a few central layers (2, 3, 6 and 12 for all A, B, C, and D interfaces, respectively). The resulting self-diffusion coefficients are compiled in Table 3.

[24] For all interfaces A to D, the atoms of crystal termination (010) show higher self-diffusion coefficients than those of the corresponding interfaces with (100) and (001) termination. By increasing the melt thickness of the same crystal surface, the self-diffusion coefficients of all species increase. The largest difference is observed between the melts of interfaces A and B with an increase in diffusivity of up to about 40%. This increase reduces to about 20% between interfaces C and D (see Table 3).

[25] Figure 5 shows profiles of the oxygen self-diffusion coefficients of interface C for different crystal orientations. Each bar represents an average over all oxygens that were present in the corresponding layer at the beginning of a 100 ps time interval. The grey areas in Figure 5 indicate the original crystal. The simulation cell lengths and hence the effective melt thickness vary slightly between different crystal surface terminations due to the different cross-sections of the crystal in (100), (010) and (001) (see Table 3). While the diffusion in the crystal part is essentially zero, a plateau is formed in the central part of the melt. For the interface with (010) crystal orientation, the self-diffusion coefficients in this central region are higher than those for the other two profiles. Also, in the (010) profile the plateau is reached more quickly away from the original contact, which indicates a smaller interfacial width. Non-zero self-diffusion in the grey areas indicates an increased ionic mobility in the first atomic layers of the crystal close to the contact with the melt. The extend of the diffusion profiles into the crystal is consistent with that of the composition fluctuations (see Figure 3), which can be explained by an

Table 3. Self Diffusion Coefficients ($\times 10^{-6} cm^2/s$) of the Three Elements (O, Si, Mg) in A, B, C and D Interfaces and for the Three Crystal Orientations (100), (010) and (001)[a]

Interface	Melt Thickness d^{tot} (nm)	Total Melt			Central Melt		
		O	Si	Mg	O	Si	Mg
A							
100	0.80	1.1(2)	0.6(2)	3.4(3)	1.1(2)	0.6(2)	4.0(2)
010	0.88	1.9(2)	1.2(2)	6.4(16)	2.0(2)	1.2(1)	8.4(14)
001	0.77	1.2(2)	0.6(2)	3.2(7)	1.2(3)	0.6(2)	4.4(3)
B							
100	1.60	1.4(2)	0.9(2)	5.9(7)	1.5(3)	1.0(2)	7.2(8)
010	1.75	2.2(2)	1.5(2)	7.4(7)	2.4(3)	1.6(3)	9.1(7)
001	1.54	1.7(2)	1.1(2)	7.1(5)	1.8(3)	1.2(2)	7.9(5)
C							
100	3.20	1.8(2)	1.2(2)	7.9(11)	2.0(2)	1.4(2)	9.2(12)
010	3.50	2.4(2)	1.7(2)	9.2(4)	2.5(2)	1.8(3)	10.0(7)
001	3.10	2.0(2)	1.3(1)	8.0(6)	2.2(2)	1.5(2)	9.3(9)
D							
100	6.40	2.2(2)	1.5(2)	8.1(7)	2.4(2)	1.7(3)	9.2(11)
010	7.00	2.6(2)	1.9(2)	9.3(2)	2.7(4)	2.1(3)	10.0(8)
001	6.20	2.3(2)	1.5(1)	8.3(5)	2.3(3)	1.6(2)	9.0(7)

[a]d^{tot} (nm) is the total melt layer thickness. The third, fourth, and fifth columns represent self-diffusion coefficients that are derived from the complete melt, whereas the sixth, seventh, and eighth columns include averaging over the central melt part only (see main text for more explanations).
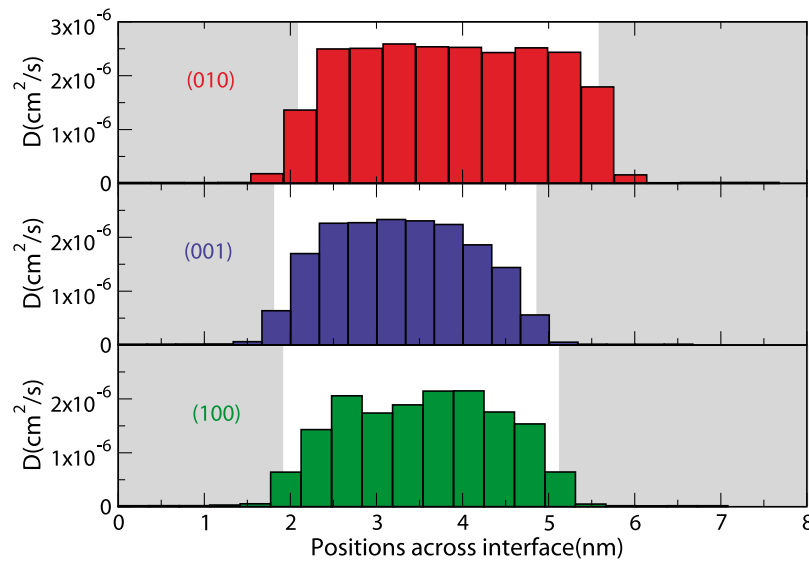
Figure 5. Self-diffusion coefficients of oxygen across the interface for crystal surface terminations (010), (001) and (100) of interface C.

increased defect density in the crystal or by the formation of a leached layer.

[26] Figure 6 shows the dependence of the oxygen self-diffusion coefficients for the different crystal terminations as a function of melt thickness. In Figure 6, both data of the complete melt and the central melt part are drawn, which shows clearly that the diffusion of the complete melt is somewhat smaller than that of the central melt part. A similar trend is observed for the Mg and Si self-diffusion coefficients (see Table 3). Averaging of the central layers gives higher self-diffusion coefficients because the electrostatic effect of crystal on the melt is better shielded away from the interface. Averaging over the complete melt also includes the region close to the interface which is less diffusive. By making the melt layer thicker, the self-diffusion coefficients converge to the pure melt value (see discussion below) and if the melt layer becomes very thin, the self-diffusion approaches that of the pure crystal, which is not observable on the timescale of our simulations.

4. Discussion and Conclusions

4.1. Structure at the Interface

[27] As shown in Figures 3 and 4, strong oscillations of structural parameters are observed in the vicinity of the initial interface. Looking at the molecular structure at the contact between melt and crystal, information on the wetting behavior can be obtained. In the present case, Mg_2SiO_4 and $MgSiO_3$ are structurally quite similar. The crystals of both systems are composed of SiO_4 tetrahedra and Mg in 6-fold octahedral coordination. The latter is reduced to an average fivefold coordination in the melt. While in Mg_2SiO_4 forsterite the SiO_4 are not connected, in $MgSiO_3$ about 2 out of 4 oxygens are bridging oxygens that connect neighboring tetrahedra. In the contact area between the two phases (see Figure 7), a partly polymerized melt meets a fully depolymerized structure. Some of the melt tetrahedra connect directly to tetrahedra of the crystal as shown in the upper part

of the interfacial region in Figure 7. In other parts, the first layer of the melt aligns parallel to the crystal surface, which leads to a fluctuating chemical composition and variations in the probability to find bridging oxygens. In contrast, the relaxation of the free surfaces as shown in Figure 2b does not result in the formation of bridging oxygens.

4.2. Relation Between Diffusion and Surface Energy

[28] All ionic species (O, Si, Mg) have higher self-diffusion coefficients in the vicinity of the (010) as compared to (100) and (001) crystal surfaces. Looking at Table 2, (010) has the lowest surface energy of the three surfaces. This
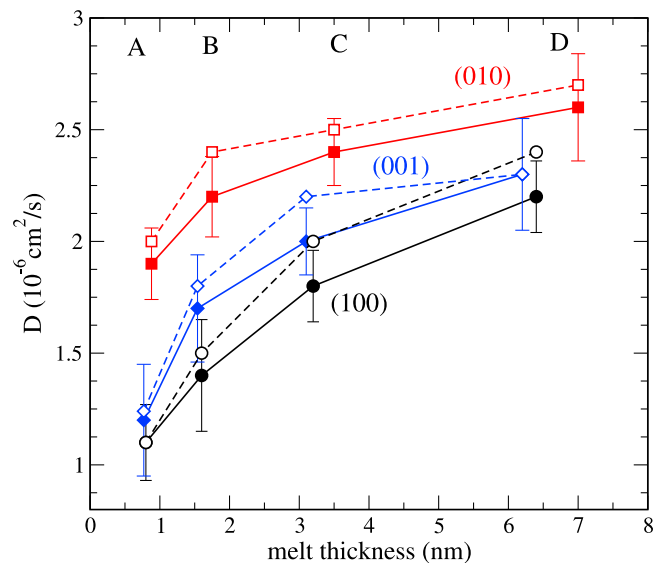

Figure 6. Self-diffusion coefficients of oxygen for different melt thickness and different surface termination. Solid symbols are for the complete melt and open symbols refer to the central melt part. Lines are a guide to the eye.
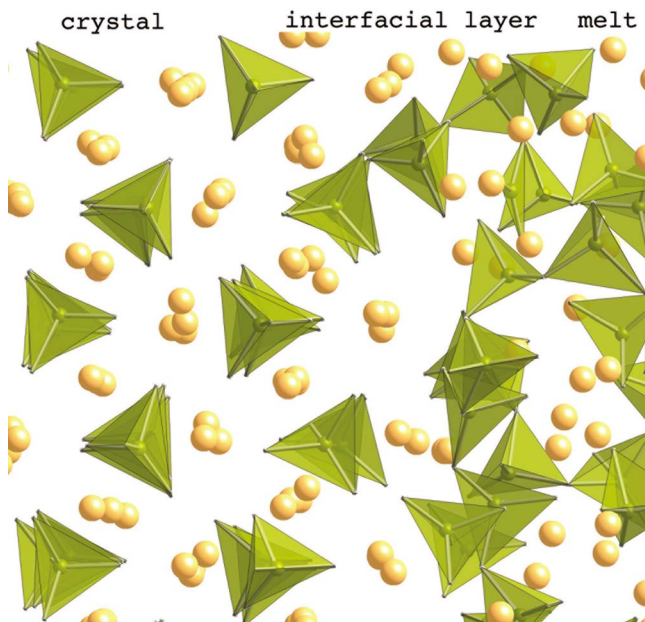
Figure 7. Snapshot of the contact area between crystal (to the left) and melt (to the right). The alignment of the first melt layer(s) with the crystal surface causes fluctuations in the structural parameters, such as the number of bridging oxygens (see Figure 4) in perpendicular direction to the interface.

suggests that there is an inverse relation between free surface energy and the mean self-diffusion coefficients of ions in the melt layer. Figure 8 shows the surface energies versus oxygen self-diffusion coefficients for the different interfaces and crystal orientations. As the surface energy increases the self-diffusion coefficient decreases. Similar behavior is observed for Mg and Si (see Table 3). The reduced ionic mobility for high surface energies can be related to the stronger interaction of the crystal surface with the melt, which leads to more structured melt close to the interface. The strong variation in surface energies (Table 2) clearly indicates that simplified dihedral angle concepts are not capable to model interfacial melt-mineral assemblages and that more complex models need to be applied [e.g., *Cmiral et al.*, 1998]. Such a study would require the computation of additional surface energies, especially of those surfaces with high Miller indices.

4.3. Extrapolation to Bulk Diffusion Coefficient and Effective Passive Layer

[29] The thickness of melt layers in partially molten rocks may be determined by transmission electron microscopy after quenching the sample to ambient pressure and temperature. Thereby it is assumed that melt layer is preserved as an amorphous layer. The thickness of this amorphous layer would be equivalent to the total thickness of the melt layer in the simulations. However, it has been shown above that not all particles of the same kind contribute equally to the respective self-diffusion coefficient. Whereas particles in the central region of the melt may be almost as mobile as those in a bulk melt, the melt atoms close to the crystal surface diffuse much less. For practical use and as a first approximation, the derived diffusion profile of the total melt

layer is divided into an active, bulk melt-like and a passive, essentially non-diffusive part. For that, we set

$$D^{tot} d^{tot} = D^{bulk} d^{eff} \qquad (2)$$

where D^{tot} and D^{bulk} are the average self-diffusion coefficients of a particle in the melt layer of the crystal-melt interface and in the corresponding bulk melt. d^{tot} is the total thickness of the melt layer in the interface and d^{eff} is the effective thickness of the active layer. D^{tot} and d^{tot} are known from Table 3. D^{bulk} is estimated from extrapolation of D^{tot} to infinite melt layer thickness, where confinement effects are negligible. A convincing extrapolation is achieved when D^{tot} is plotted over the inverse square root of the melt layer thickness (see Figure 9). The 480 atom simulation cell of pure $MgSiO_3$ melt has a slightly higher diffusivity than the confined melts but due to the relatively small simulation cell, finite size effects are apparent. A summary of the extrapolated D^{bulk} is given in Table 4.

[30] The thickness of the passive layer $d^{passive}$ of one crystal-melt interface is then given by

$$d^{passive} = \left(d^{tot} - d^{eff}\right)/2 \qquad (3)$$

Note that there are two interfaces and therefore two passive layers. The evolution of the passive layer thickness as a function of total melt layer thickness is shown for oxygen in Figure 10. After a significant initial increase, a plateau is reached for thick melt layers. The data is well described by the empirical relation

$$d^{passive} = d^{passive}_{\infty}(1 - \exp(-kd^{tot})) \qquad (4)$$

where $d^{passive}_{\infty}$ is the maximum thickness of the passive layer for thick melt layers and k is a constant. All fitted $d^{passive}_{\infty}$ and
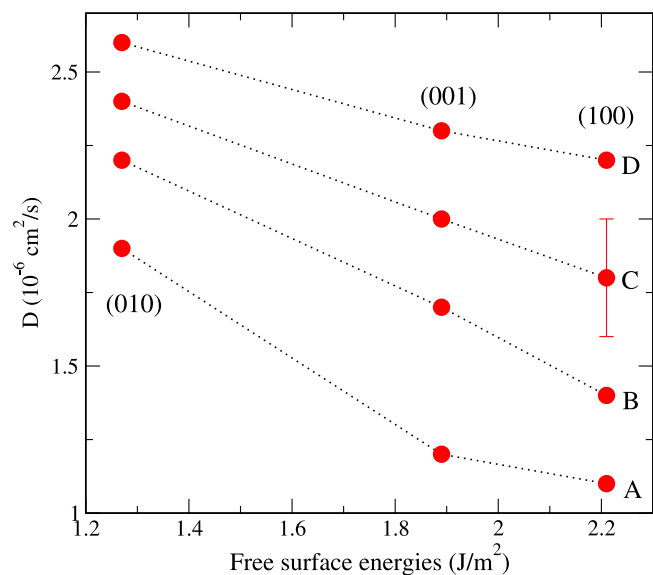

Figure 8. Oxygen self-diffusion coefficients for different crystal surface terminations and melt layer thickness (interfaces A to D) with respect to free surface energies. All errors are in the same order as indicated for (100) of interface C. The dotted lines are a guide to the eye.
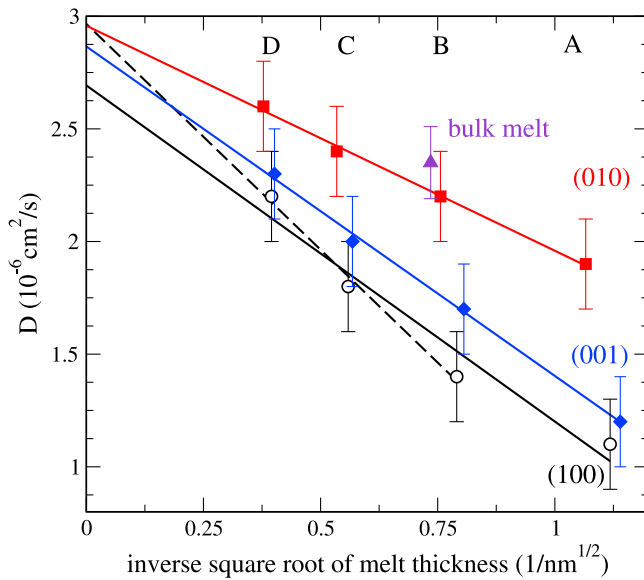
Figure 9. Linear regression to self-diffusion coefficients of oxygen (all melt data of Table 3) plotted against the inverse square root of the total melt layer thickness. The dashed line refers to the (100) interfaces B to D only.

k are listed in Table 4. We also attempted a self-consistent global fit of the self-diffusion data as a function of the total melt thickness by combining equations (2) to (4) but the small number of data points and their relatively large uncertainty resulted in large ambiguities of the fitted parameters. Within these uncertainties, however, those parameters were consistent with the results presented in Table 4.

[31] For thick melt pockets, the interfacial melt layer that has to be considered immobile is in the range of about 0.4 to 1.0 nm depending on the crystal surface termination. Although this thickness reduces for ultrathin films of only a few nanometers, its relative importance increases significantly. While for a total melt film of about 7 nm, the two passive layers comprise about 12% (010) to 24% (100) of the total melt thickness, these values increase to about 35% (010) to 60% (100) for a 1 nm thick melt. Thus, in the latter

case the effective ionic mobility is reduced to half of that of the corresponding bulk melt.

4.4. Implications

[32] The electrical conductivity of the bulk melt can be estimated by inserting the extrapolated self-diffusion coefficients D^{bulk} (as substitute of the unknown conductivity diffusion coefficient) into the Nernst-Einstein equation

$$\sigma = \frac{e^2 n}{k_B T} \sum_i z_i^2 c_i D_i^{bulk} \tag{5}$$

where e is the electronic charge, n the particle density of the melt, k_B the Boltzmann constant, z_i the nominal charge of ion i (−2 for oxygen, +2 for Mg, +4 for Si) and c_i the concentration of element i (0.6 for oxygen, 0.2 for Mg and Si). The particle density of 7.66×10^{28} m^{-3} was obtained from the molecular dynamics simulation of the 480 ion bulk melt. Using average D^{bulk} of 11.2×10^{-6} cm^2/s, 2.1×10^{-6} cm^2/s and 2.9×10^{-6} cm^2/s for Mg, Si and O, an electrical conductivity of 161 S/m is obtained. The corresponding partial contributions are 64 S/m (40%) for Mg, 48 S/m (30%) for Si and 49 S/m (30%) for O.

[33] The calculated electrical conductivity of the melt is consistent with experimental data of *ten Grotenhuis et al.* [2005]. Extrapolation of their bulk melt conductivities to 2000 K gives a slightly lower value of about 130 S/m. The estimated conductivity from the simulation probably constitutes an upper limit since blocking and correlation effects were not taken into account and all particles were treated as purely ionic. Our results suggest that for MgSiO$_3$ melt, all ionic species contribute almost equally to the electrical conductivity.

[34] In rocks with very thin melt films as they are expected as initial melts [*Wirth*, 1996] or under well wetting conditions, the thin interfacial layer may contribute significantly to the overall conductivity. In partially molten rocks, the
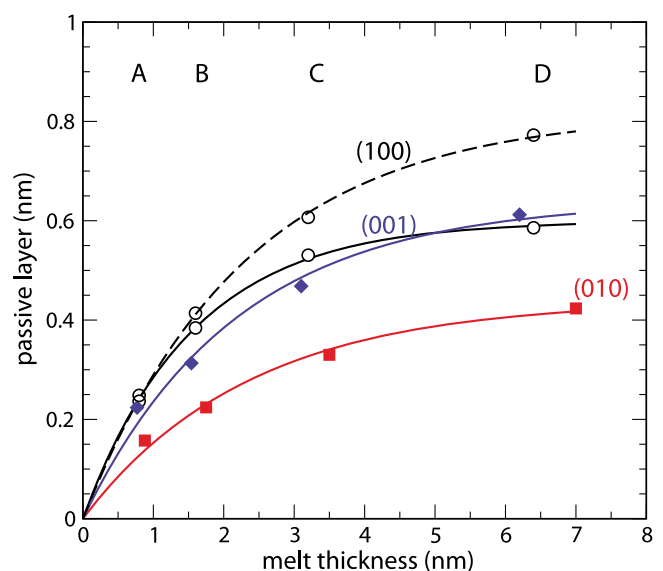
Table 4. Extrapolated Self-Diffusion Coefficients for Bulk Melt (10^{-6} cm^2/s), Thickness of the Passive Layer (nm), and k Fitting Parameter of Equation (4) (1/nm)[a]

	Surface	D^{bulk}	$d_\infty^{passive}$	k
	(100)	2.69	0.60	0.64
	(100)[b]	2.97	0.82	0.44
O	(010)	2.96	0.44	0.43
	(001)	2.87	0.64	0.46
	(100)	1.92	0.72	0.57
	(100)[b]	2.07	0.95	0.41
Si	(010)	2.26	0.58	0.43
	(001)	2.00	0.85	0.36
	(100)	11.2		
Mg	(010)	11.2		
	(001)	11.7		

[a]Due to the relatively large errors in Mg self-diffusion coefficients (see Table 3), no meaningful estimation of $d_\infty^{passive}$ and k for Mg could be obtained.

[b]Regression line fitted only to interfaces B to D.

Figure 10. Thickness of the passive layer of oxygen as a function of total melt layer thickness. The symbols and line styles correspond to those in Figure 9.

electrical conductivity is mainly limited by the smallest junction of the melt. Considering the reduced self-diffusion coefficients for the ultrathin melt films studied here, the reduction in electrical conductivity or the anisotropy of the electrical conductivity in aggregates with preferred orientations should not exceed a factor of two if caused by interfacial layers only. Potentially, such simulations of partially molten rocks could be extended to sample the phase behavior and to study differentiation processes in model systems at varying $P - T$ conditions but also for different chemical composition.

References

Adjaoud, O., G. Steinle-Neumann, and S. Jahn (2008), Mg_2SiO_4 liquid under high pressure from molecular dynamics, *Chem. Geol.*, *256*, 184–191.

Alba-Simionesco, C., B. Coasne, G. Dosseh, G. Dudziak, K. E. Gubbins, R. Radhakrishnan, and M. Sliwinska-Bartkowiak (2006), Effects of confinement on freezing and melting, *J. Phys. Condens. Matter*, *18*, R15–R68.

Alcoutlabi, M., and G. B. McKenna (2005), Effects of confinement on material behaviour at the nanometre size scale, *J. Phys. Condens. Matter*, *17*, R461–R524.

Alfe, D. (2005), Melting curve of MgO from first-principles simulations, *Phys. Rev. Lett.*, *94*, 235701.

Allen, M. P., and D. Tildesley (1987), *Computer Simulation of Liquids*, Oxford Univ. Press, Oxford, U. K.

Baba, K., A. D. Chave, R. L. Evans, G. Hirth, and R. L. Mackie (2006), Mantle dynamics beneath the East Pacific Rise at 17°S: Insights from the mantle electromagnetic and tomography (melt) experiment, *J. Geophys. Res.*, *111*, B02101, doi:10.1029/2004JB003598.

Belonoshko, A. B., and L. S. Dubrovinsky (1996), Molecular dynamics of NaCl (B1 and B2) and MgO (B1) melting: Two-phase simulation, *Am. Mineral.*, *81*, 303–316.

Bertaut, F. (1958), The electrostatic term of the surface energy, *C. R. Acad Sci.*, *246*, 3447–3450.

Bowen, N. L., and O. Andersen (1914), The binary system $MgO-SiO_2$, *Am. J. Sci.*, *37*, 487–500.

Brasse, H., and D. Eydam (2008), Electrical conductivity beneath the Bolivian Orocline and its relation to subduction processes at the South American continental margin, *J. Geophys. Res.*, *113*, B07109, doi:10.1029/2007JB005142.

Cmiral, M., J. D. Fitz Gerald, U. H. Faul, and D. H. Green (1998), A close look at dihedral angles and melt geometry in olivine basalt aggregates: A TEM study, *Contrib. Mineral. Petrol.*, *130*, 336–345.

de Kloe, R., M. R. Drury, and H. L. M. van Roermund (2000), Evidence for stable grain boundary melt films in experimentally deformed olivine-orthopyroxene rocks, *Phys. Chem. Miner.*, *27*, 480–494.

Drury, M. R., and J. D. Fitz Gerald (1996), Grain boundary melt films in an experimentally deformed olivine-orthopyroxene rock: Implications for melt distribution in upper mantle rocks, *Geophys. Res. Lett.*, *23*(7), 701–704, doi:10.1029/96GL00702.

Eaton, D. W., F. Darbyshire, R. L. Evans, H. Grutter, A. Jones, and X. Yuan (2009), The elusive lithosphere-asthenosphere boundary (LAB) beneath cratons, *Lithos*, *109*, 1–22.

Faul, U. H., J. D. Fitz Gerald, and I. Jackson (2004), Shear wave attenuation and dispersion in melt-bearing olivine polycrystals: 2. Microstructural interpretation and seismological implications, *J. Geophys. Res.*, *109*, B06202, doi:10.1029/2003JB002407.

Fujino, K., S. Saaski, Y. Takeuchi, and R. Sadanaga (1981), X-ray determination of electron distributions in forsterite, fayalite and tephroite, *Acta Crystallogr., Sect. B Struct. Crystallogr. Cryst. Chem.*, *37*, 513–518.

Hess, P. C. (1994), Thermodynamics of thin fluid films, *J. Geophys. Res.*, *99*, 7219–7229.

Hiraga, T., I. M. Anderson, and D. L. Kohlstedt (2003), Chemistry of grain boundaries in mantle rocks, *Am. Mineral.*, *88*, 1015–1019.

Jahn, S. (2010), Integral modeling approach to study the phase behavior of complex solids: Application to phase transitions in $MgSiO_3$ pyroxenes, *Acta Crystallogr., Sect. A Cryst. Phys. Diffr. Theor. Gen. Crystallogr.*, *66*, 535–541.

Jahn, S., and P. A. Madden (2007), Modeling earth materials from crustal to lower mantle conditions: A transferable set of interaction potentials for the CMAS system, *Phys. Earth Planet. Inter.*, *162*, 129–139.

Jahn, S., and R. Martoňák (2008), Plastic deformation of orthoenstatite and the ortho- to high-pressure clinoenstatite transition: A metadynamics simulation study, *Phys. Chem. Miner.*, *35*, 17–23.

Jahn, S., and R. Martoňák (2009), Phase behavior of protoenstatite at high pressure studied by atomistic simulations, *Am. Mineral.*, *94*, 950–956.

Kohlstedt, D. H., and M. E. Zimmerman (1996), Rheology of partially molten mantle rocks, *Annu. Rev. Earth Planet. Sci.*, *24*, 41–62.

Kohlstedt, D. L., and B. K. Holtzman (2009), Shearing melt out of the Earth: An experimentalist's perspective on the influence of deformation on melt extraction, *Annu. Rev. Earth Planet. Sci.*, *37*, 561–593.

Lange, R. A., and I. S. E. Carmichael (1987), Densities of $Na_2O-K_2O-CaO-MgO-Fe_2O_3-Al_2O-TiO_2-SiO_2$ liquids: New measurements and derived partial molar properties, *Geochim. Cosmochim. Acta*, *51*, 2931–2946.

Lanning, O. J., S. Shellswell, and P. A. Madden (2004), Solid–liquid coexistence in ionic systems and the properties of the interface, *Mol. Phys.*, *102*, 839–855.

Madden, P. A., R. Heaton, A. Aguado, and S. Jahn (2006), From first-principles to material properties, *J. Mol. Struct. THEOCHEM*, *771*, 9–18.

Martyna, G. J., D. J. Tobias, and M. L. Klein (1994), Constant pressure molecular dynamics algorithms, *J. Chem. Phys.*, *101*, 4177–4189.

Nosé, S., and M. L. Klein (1983), Constant pressure molecular dynamics for molecular systems, *Mol. Phys.*, *50*, 1055–1076.

Partzsch, G. M., F. R. Schilling, and J. Arndt (2000), The influence of partial melting on the electrical behavior of crustal rocks: Laboratory examinations, model calculations and geological interpretations, *Tectonophysics*, *317*, 189–203.

Roberts, J. J., and J. A. Tyburczy (1999), Partial melt electrical conductivity: Influence of melt composition, *J. Geophys. Res.*, *104*(B4), 7055–7065.

Schmeling, H. (1985), Numerical models on the influence of partial melt on elastic, anelastic and electrical properties of rocks. Part 1: Elasticity and anelastcity, *Phys. Earth Planet. Inter.*, *41*, 34–57.

Schmeling, H. (1986), Numerical models on the influence of partial melt on elastic, anelastic and electrical properties of rocks. Part 2: Electrical conductivity, *Phys. Earth Planet. Inter.*, *43*, 123–136.

ten Grotenhuis, S. M., M. R. Drury, C. J. Peach, and C. J. Spiers (2004), Electrical properties of fine-grained olivine: Evidence for grain boundary transport, *J. Geophys. Res.*, *109*, B06203, doi:10.1029/2003JB002799.

ten Grotenhuis, S. M., M. R. Drury, C. J. Spiers, and C. J. Peach (2005), Melt distribution in olivine rocks based on electrical conductivity measurements, *J. Geophys. Res.*, *110*, B12201, doi:10.1029/2004JB003462.

Waff, H. S., and J. R. Bulau (1979), Equilibrium fluid distribution in an ultramafic partial melt under hydrostatic stress conditions, *J. Geophys. Res.*, *84*(B11), 6109–6114.

Waff, H. S., and J. R. Bulau (1982), Experimental determination of near-equilibrium textures in partially molten silicates at high pressures, *Adv. Earth Planet. Sci.*, *12*, 229–236.

Waff, H. S., and U. H. Faul (1992), Effects of crystalline anisotropy on fluid distribution in ultramafic partial melts, *J. Geophys. Res.*, *97*(B6), 9003–9014.

Watson, G. W., P. M. Oliver, and S. C. Parker (1997), Computer simulation of the structure and stability of forsterite surfaces, *Phys. Chem. Miner.*, *25*, 70–78.

Wirth, R. (1996), Thin amorphous films (1–2 nm) at olivine grain boundaries in mantle xenoliths from San Carlos, Arizona, *Contrib. Mineral. Petrol.*, *124*, 44–54.

Yoshino, T., D. Yamazaki, and K. Mibe (2009), Well-wetted olivine grain boundaries in partially molten peridotite in the asthenosphere, *Earth Planet. Sci. Lett.*, *283*, 167–173.

H. Brasse, Fachrichtung Geophysik, Freie Universität Berlin, Malteserstr. 74-100, D-12249 Berlin, Germany. (heinrich.brasse@fu-berlin.de)

S. F. Gurmani and S. Jahn, Section 3.3, German Research Centre for Geosciences, Telegrafenberg, D-14473 Potsdam, Germany. (samia.gurmani@gfz-potsdam.de; sandro.jahn@gfz-potsdam.de)

F. R. Schilling, Institut für Angewandte Geowissenschaften, Karlsruhe Institute of Technology, D-76128 Karlsruhe, Germany. (frank.schilling@kit.edu)